PAPER

Dynamic adsorption of toluene on amino-functionalized SBA-15 type spherical mesoporous silica

Huiping Zhou,[a] Shaomin Gao,[a] Wenwen Zhang,[b] Zhaohui An[a] and Donghui Chen (ID) *[ab]

Amino-functionalized spherical mesoporous silica (ASMS) materials were successfully prepared *via* a convenient treatment method by using 3-aminopropyltrimethoxysilane (APTES), which was used in different concentrations in the process of spherical mesoporous silica (SMS) synthesis. The adsorption performances of ASMS were evaluated by taking toluene as a simulated pollutant and the adsorption mechanism was also studied. A variety of characterization methods were adopted, including scanning electron microscopy, small-angle X-ray diffraction and Fourier-transform infrared spectroscopy techniques and nitrogen adsorption–desorption analyses, which led to a better understanding of the performance of the materials. It was found that the SMS has a good adaptability due to the amino functionality, the pore structure still remains in the modified samples even when the mass ratio of APTES/TEOS is up to 3, and the chemical properties of the material surface are significantly improved by the amino functionality. The results show that the capacities of the toluene adsorption follow the order of SMS < ASMS-1 < ASMS-3 < ASMS-2. ASMS-2 has the highest toluene adsorption capacity (98.1 mg g^{-1}) and the saturated adsorbent can be easily regenerated by thermal desorption, which has a stable adsorption capacity after 4 adsorption cycles. These experimental data indicated that amino functionalization could affect both the pore structure and surface chemical properties of SMS, making ASMS a promising material for the reduction of industrial volatile organic compound emissions in air treatment.

1. Introduction

Volatile organic compounds (VOCs) are increasingly becoming well known for their toxicity and their impact on the environment, even at low concentrations.[1] VOCs can easily evaporate into the atmosphere due to their high vapor pressure, reacting with nitrogen oxides in sunlight to form ozone and photochemical oxidants, and both secondary organic aerosol[2–4] and photochemical ozone are affected by VOCs in air pollution. More importantly, VOCs are also harmful to human organs, including lungs, liver and kidneys, the nervous system and respiratory system and can even cause cancer.[5,6] So, it is urgent to control VOC emissions to alleviate environmental threats.[7]

There are many technologies commercially available for the treatment of VOCs including adsorption,[8,9] catalytic oxidation,[10,11] absorption technology, biological treatment,[12,13] and plasma degradation,[14] as well as other techniques based on these methods. Examples are adsorption–condensation,[15] adsorption

condensation–catalytic oxidation,[16,17] adsorption–photocatalysis,[18,19] adsorption–absorption,[20] and plasma-photocatalysis technologies.[21,22] These composite techniques were used to adapt the complexity of exhaust gas components and properties of VOCs to avoid the limitations of a single treatment technology. Obviously, the adsorption method has a very important position among the various treatment techniques of VOCs. Compared with other methods, absorption technology has high technical requirements for equipment which is susceptible to corrosion and the absorbent needs to be replaced regularly, making the operating costs increase. Although catalytic oxidation is relatively economic for its low operating temperature, the combustion products produced by the VOCs during the combustion process and the catalyst after the reaction require secondary treatment,[23] and catalytic oxidation technology is not suitable for treating exhaust gases containing sulphur, nitrogen and halides. Biological treatment is highly economical in the treatment of low-concentration and biodegradable VOCs; however, conditions such as temperature, pH, and nutrients that satisfy the growth and reproduction of microorganisms are difficult to control. Expectantly, based on the high selectivity of the adsorbent, adsorption technology can treat gas mixtures that are difficult to separate by other processes, thereby effectively removing and recovering harmful substances with low concentration; there is not only no secondary pollution, but also

[a]School of Chemical and Environmental Engineering, Shanghai Institute of Technology, Haiquan Road 100, 201418, Shanghai, PR China. E-mail: 1019138856@qq.com

[b]College of Environmental Science and Engineering, Donghua University, North Renmin Road 2999, 201620, Shanghai, PR China. E-mail: chendhsit@163.com

high purification efficiency. With the rapid development of adsorption technology and processes and the development of new adsorbents, adsorption technology has become an important chemical process, especially in the field of organic gas separation, purification, recovery, *etc.*

The core issue in the process of VOC adsorption is to find suitable and efficient adsorbents.[24] In the VOC adsorption process, common adsorbents include carbon,[25–27] silica gel,[28,29] metal–organic frameworks,[30–32] molecular sieves,[33–35] *etc.* Among them, mesoporous molecular sieves have a wide range of application prospects in the treatment of pollution due to their high specific surface area which can be easily adjusted.[36] As a typical representative of mesoporous materials, SBA-15 has attracted the attention of scientific researchers since 1998, when first prepared by Zhao. This type of mesoporous silica material can be synthesized using a soft template method, using a block-type surfactant and its pore size is adjustable in the range of 5–30 nm.[37] Due to the thicker pore wall of SBA-15, the hydrothermal stability of the material is better than that of the MCM and KIT series of materials. In a calcining process, the surfactant embedded in the pore wall can be removed to generate a microporous structure. Therefore, SBA-15 is a multi-dimensional porous material containing micropores and mesopores, which has been applied in many research fields, including biosensors,[38] CO_2 capture,[39] heavy-metal ion removal,[40] drug release,[41] *etc.* Although numerous studies have certified SBA-15 as an adequate adsorbent in environmental remediation, its applications in VOC adsorption have not been well studied previously.[42]

In this study, amino-functionalized spherical mesoporous silica (ASMS) samples were successfully synthesized by a convenient method whereby chemical groups were grafted onto SBA-15 by 3-aminopropyltrimethoxysilane (APTES) at different concentrations. Toluene is a typical representative VOC and, although its toxicity is much lower than that of benzene, it is still harmful to human health at high concentrations. Therefore, toluene was used as a simulated pollutant in this work. By comparing the adsorption capacity of toluene on the obtained material, the dynamic adsorption performance and the related adsorption mechanism were studied. Results indicate that both the structure and surface chemical properties of SMS were affected by the amino functionality, and the ASMS-2 material shows the highest VOC adsorption capacity, strong recyclability and has good potential for VOC removal.

2. Experimental section

2.1 Raw materials and chemicals

Chemicals used in this experiment include the triblock copolymer $EO_{20}PO_{70}EO_{20}$ (Pluronic P123, MW = 5800), tetraethyl orthosilicate (TEOS, 99.5%), APTES (99%), hydrochloric acid (HCl, 37%), and ethanol (99.7%). All chemicals were obtained commercially and used without further purification.

2.2 Preparation of SMS

According to the work detailed by Zhao[37] and colleagues, pure SBA-15 material (SMS) was successfully synthesized. A certain amount of P123 and HCl solution was mixed in a round-bottom flask and stirred continuously at 45 °C until the solution was clear and transparent. Then, a certain volume of TEOS was slowly added dropwise, continuing stirring for 15 min and let stand for 20 h. The mixture, which turned milky white, was moved into a Teflon reaction container and placed in a 100 °C oven for 24 h. After removal from the Teflon reaction container, the mixture was collected by filtration and washed until the pH of the washing liquid was near neutral, then the white solid was dried at 100 °C overnight. The template was removed by calcining in a tubular furnace in which the temperature was raised to 550 °C at 5 °C min^{-1} and kept for 6 h. The obtained sample was designated as SMS. The chemical composition of the reaction mixture was 4 g P123, 9.14 mL TEOS and 120 mL HCl (2 M).

2.3 Preparation of ASMS

The SMS sample (1 g) was added to 50 mL of ethanol (99.7%) and magnetically stirred at room temperature for 2 h. Afterward, a certain mass ratio of SMS and APTES (where the mass ratios of TEOS/APTES were 1 : 1, 1 : 2 and 1 : 3) was dissolved in 50 mL ethanol. The mixture was then heated at 75 °C for 12 h under cold water circulation conditions. ASMS was obtained after filtering, washing, and drying, named ASMS-1, ASMS-2 and ASMS-3, respectively.

2.4 Adsorbent characterizations

Structural studies and morphological analysis of as-obtained samples were achieved by scanning electron microscopy (SEM, Hitachi S-4800). The crystal structure and phase of the as-obtained original and functionalized mesoporous silicas were identified using small-angle X-ray diffraction (XRD, Mini Flex600) between 1° and 10°. Adsorption–desorption isotherms of nitrogen were measured with a NOVA 1200 gas sorption analyzer at −196 °C. The specific surface area and pore size were also analyzed. Before characterization, all of the samples were dried under vacuum at 105 °C for 12 h. The specific surface area was calculated using the Brunauer–Emmett–Teller (BET) method from the adsorption data obtained in the range of 0.04–0.32 relative pressure (P/P_0) and the total pore volume was estimated from the amount of adsorption at a relative pressure of about 0.98. According to the Barrett–Joyner–Halenda (BJH) algorithm, the pore size distribution curve was calculated by analyzing the desorption branch of the isotherm. The micropore volume and micropore surface area were estimated using the *t*-plot method. In addition, elemental analyses of SMS and ASMS were conducted by energy dispersive X-ray spectroscopy (EDX, 4500H), and Fourier-transform infrared (FTIR) spectroscopy was used with the KBr method across a scanning range of 4000–400 cm^{-1}.

2.5 Dynamic adsorption experiments

Under gas flow conditions, dynamic toluene adsorption was investigated. A 0.1 g sample, which was ground and divided into 40 to 60 mesh particles with sieves, was loaded into a fixed bed reactor. The sample was dried under vacuum at 105 °C overnight and then taken to the adsorption experiment, in order to eliminate the interference of physically adsorbed water

molecules and a small amount of volatile organic impurities. Specifically, the exhaust gas initial concentration (C_0, mg L^{-1}) of simulated toluene was 2 mg L^{-1} in this experiment, and the adsorption operation was carried out under dry conditions. For ease of comparison, both the original sample and the amino-functionalized mesoporous silica were subjected to dynamic adsorption of toluene in the experimental apparatus (as indicated in Fig. 1). Nitrogen was used as a carrier gas for the purpose of controlling the total flow rate at 60 mL min^{-1}. Determining the amount of adsorption was achieved by using a gas chromatograph (GC) of the FID type to test the concentration changes before and after the adsorption experiment. The catheters for the circulation of toluene gas were 3 mm stainless steel tubes that were heated at 60 °C.

The toluene adsorption capacity (q, mg g^{-1}) of ASMS was calculated from the breakthrough curves based on eqn (1):

$$q = \frac{M}{1000m} \int_0^{t_1} Q(C_0 - C_t)\mathrm{d}t \tag{1}$$

where Q (mL min^{-1}) is the gas flow rate, C_0 and C_t (mol L^{-1}) are the initial concentration and real-time outlet concentration of toluene, respectively, t_1 (min) is the breakthrough time when $C_t = C_0$, m (g) is the mass of the adsorbent, and M is the molar mass of toluene, the value of which is 92.14 g mol^{-1}. The breakthrough curves were fitted using the Yoon and Nelson model[43] as shown in eqn (2):

$$t = \tau + \frac{1}{k} \ln(C_t/(C_0 - C_t)) \tag{2}$$

where t (min) is the breakthrough time, τ (min) is the time when $C_t = 0.5C_0$, and k is a rate constant related to the diffusion and mass transfer.

In order to study the regenerability of ASMS, *in situ* desorption and cycling experiments were carried out on materials that had adsorbed toluene. Briefly, after the toluene was dynamically adsorbed on the ASMS material, the physically adsorbed toluene was desorbed at 105 °C with a flow rate of N$_2$ gas until the detected toluene concentration was less than 10 ppm. Then, another adsorption test cycle was carried out in accordance with the operation of the above dynamic adsorption experiment.

3. Results and discussion

3.1 Characterization of samples

It can be seen that both SMS and ASMS presented a spherical morphology with diameters from 2 to 5 mm. Although SMS

Fig. 1 Schematic diagram for the dynamic adsorption of toluene.

(Fig. 2a) and ASMS (Fig. 2b–d) were calcined at 550 °C for 6 h, all of them kept their spherical morphology. The morphology of SMS modified by different APTES contents did not change significantly, showing a complete spherical shape. However, since the reflow process is carried out under different concentrations of APTES, this caused different degrees of rough surface to appear on the surface of the originally smooth silicon spheres, which also has different manifestations in the adsorption effect of VOCs. Table 1 presents the content of elements before and after the modification of samples, as measured by EDX, and it was found that the content of N element increased with the addition of APTES, which also confirmed that the surface of the SMS was indeed loaded with amino groups. In addition, this provides data support for explaining the XRD and BET phenomena by using the channel blockage.

The structures of samples were characterized by small-angle XRD in the range of $2\theta < 10°$, and the XRD patterns of SMS and ASMS are shown in Fig. 3, which indicated their crystalline structure. An obvious intense peak was observed at $2\theta \approx 1.2°$,
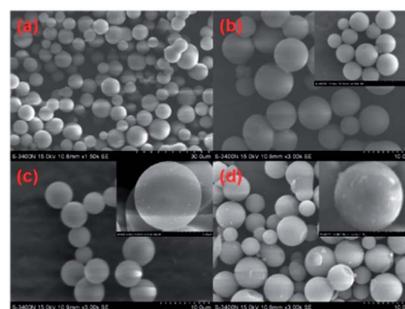

Fig. 2 SEM images of (a) SMS (×1500), (b) ASMS-1 (×3000), (c) ASMS-2 (×3000), and (d) ASMS-3 (×3000).

Table 1 Elemental analysis of SMS and ASMS

Sample	Element content (wt%)				Experimental N (mmol g^{-1})
	Si	N	O	H	
SMS	47.7	0.9	49.4	2	—
ASMS-1	38.3	12.4	42.2	7.1	8.9
ASMS-2	36.6	15.2	39.3	8.9	10.9
ASMS-3	34.5	17.1	35.7	12.7	12.2
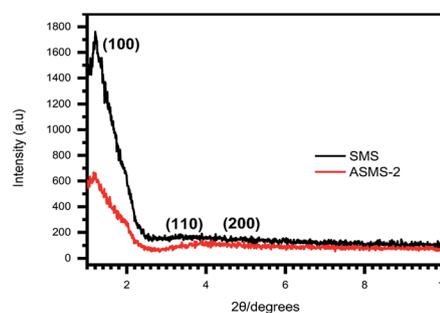
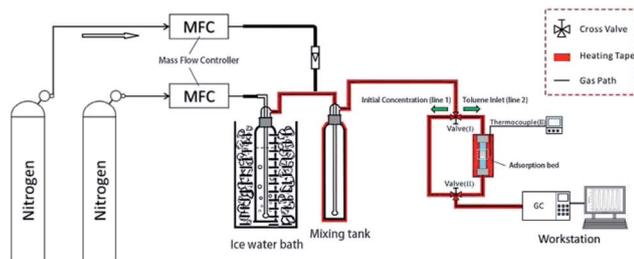Fig. 3 X-ray diffraction patterns in the small-angle range of SMS and ASMS-2.

which is characteristic of a hexagonal pore arrangement. In addition, according to the characteristics of *P6mm* structure, the three peaks present in the range of $2\theta \approx 1$–$10°$ can be described as the planes (100), (110) and (200), which is consistent with previous research results. For ASMS-2, three diffraction peaks can still be observed, but the intensity of each diffraction peak is reduced compared with the original SMS sample. This could be explained in terms of the mesopores being filled with amino groups, which leads to a decrease in the scattering contrast between the channel and the wall of the pore after the modification by amino groups,[44,45] which coincided with the SEM results.

The infrared spectral analysis results of the SMS and ASMS samples are shown in Fig. 4. It can be obviously noticed that there are two peaks at 803 cm^{-1} and 1065 cm^{-1}, which were caused by the symmetric vibration and the asymmetric vibration of Si–O–Si bonds, respectively. Additionally, the ASMS samples show a wider absorption peak near 3482 cm^{-1} in comparison to heir SMS counterpart, which is related to the stretching vibration of the Si–OH group. The hydroxyl-group bending vibration caused by physically adsorbed water corresponds to the peak at 1633 cm^{-1}, and the intensity of the absorption peak of ASMS at 1633 cm^{-1} is significantly reduced, indicating that the ability of the modified material to adsorb water is reduced. This could be a result of partially hydrophilic Si–OH on the surface of the SMS being replaced by the hydrophobic –Si(CH$_2$)$_3$NH$_2$, resulting in a decrease in the hydrophilicity of the SMS, which means the hydrophobicity of the ASMS is improved.[46] Although mesoporous silica molecular sieves are made up of three types of silanol, silylation reaction occurs between the coupling agent and two of the silanol groups (–SiOH and Si–OH). Compared with SMS, three additional absorption peaks of ASMS are clearly visible at 693 cm^{-1}, 1541 cm^{-1}, and 2938 cm^{-1}.[47] The peak at 2938 cm^{-1} can be interpreted as the vibration peak for C–H stretching from CH$_2$ or CH$_3$.[48] Furthermore, the two absorption peaks occurring at 693 cm^{-1} and 1541 cm^{-1} correspond to the bending vibration peak of N–H and the symmetrical vibration peak of –NH$_3^+$, respectively. All these infrared spectral analysis results confirm that the amino groups were successfully grafted onto the surface of the ASMS materials.[49]

Nitrogen adsorption–desorption was used to investigate the porosity and specific surface area of the as-obtained samples. As shown in Fig. 5a, the adsorption–desorption isotherms shown
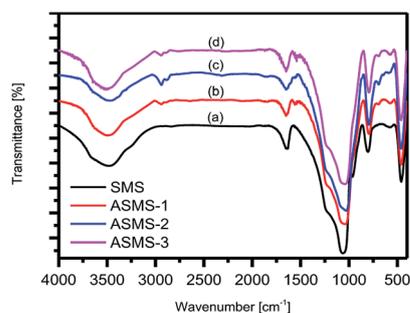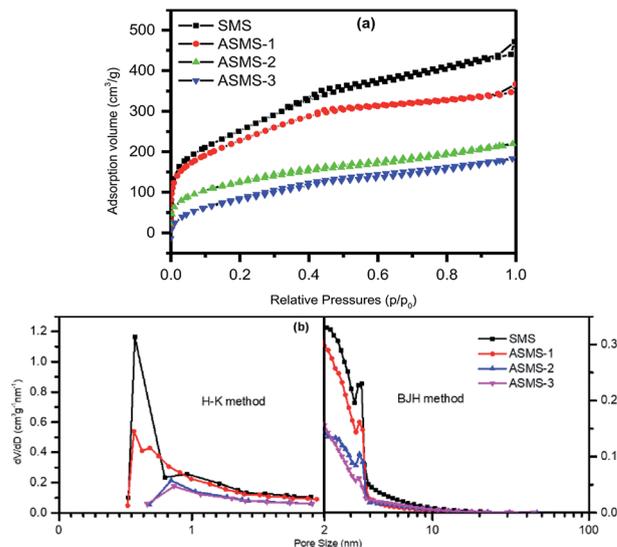

Fig. 5 (a) Nitrogen adsorption–desorption isotherms and (b) corresponding pore size distributions of the ASMS samples.

by SMS and ASMS-1 belong to type IV, indicating relatively few mesopores in the samples. Compared with SMS, the adsorption capacities of ASMS-1, ASMS-2, and ASMS-3 slightly reduced after amino functionalization with APTES, which reveals that the porous structure of the materials was changed due to the amino functionalization.

It can be noticed that the adsorption volume of ASMS-2 and ASMS-3 obviously increased at a relatively low pressure ($P/P_0 < 0.4$) and these data correspond to the adsorption isotherms of type I, which accorded with microporous characteristics. As for relevant pore size distribution, most of the micropore diameters concentrate on 0.7 and 0.9 nm (calculated by H–K method), and the mesopore diameters mainly focus on 2.8 nm (calculated by BJH method). The pore size distribution measured by density functional theory is shown in Fig. 5b, and all samples exhibit mesoporous distribution (2 nm to 5 nm).

Table 2 lists the textural parameters of the samples. Obviously, SMS has the highest nitrogen adsorption capacity and the biggest S_{BET} (approximately 915 m^2 g^{-1}). After grafting amino groups onto the adsorbent surface, it can be observed that the S_{BET} of the material dramatically decreases (down to 458 m^2 g^{-1}), and V_p and D_a calculated by the BJH method have decreased accordingly, which indicates that the amino groups are indeed grafted into the pores of SMS. This can be explained in that the larger aminopropyl groups enter the pores and produce a certain steric hindrance effect due to the increasing content of amino groups (Table 1), resulting in uneven distribution in the pores and blockage of the pores.[50]

3.2 Dynamic adsorption of VOCs

Previous studies have confirmed that the composition, porous structure and surface properties of an adsorbent all might lead to different VOC adsorption properties. In this paper, for evaluating the dynamic adsorption performance of the adsorbents, breakthrough measurement was used in a continuous toluene

Fig. 4 FTIR spectra of (a) SMS, (b) ASMS-1, (c) ASMS-2, and (d) ASMS-3.

Table 2 Textural parameters of amino-functionalized spherical mesoporous silica (ASMS)

	Textural properties				
Sample	$S_{BET}{}^a$ [m^2 g^{-1}]	$S_{micro}{}^b$ [m^2 g^{-1}]	$V_{micro}{}^c$ [m^3 g^{-1}]	$V_p{}^d$ [m^3 g^{-1}]	$D_a{}^e$ [nm]
SMS	914.7488	726.38	0.43539	0.7295	3.1899
ASMS-1	817.6741	732.89	0.42137	0.5679	2.7781
ASMS-2	459.916	342.5	0.1873	0.3395	2.9527
ASMS-3	458.6152	366.59	0.21727	0.3433	2.9942

[a] The specific surface areas were calculated using the BET method. [b] Micropore surface area from the *t*-plot meod. [c] Micropore volume determined by the *t*-plot method. [d] Total pore volume at $P/P_0 \sim 0.99$. [e] Average pore diameter.

adsorption process.[51] Fig. 6 shows the dynamic adsorption isotherms of toluene on the obtained samples at 35 °C and the Yoon–Nelson model was used to fit these curves.[52,53] The breakthrough curves can be divided into three phases during the 120 min test. Only a small amount of toluene was detected in the first stage and C/C_0 was negligible, which indicated that the adsorption of toluene by ASMS could be a fast and almost entirely adsorption-based process. In general, the C/C_0 value of the curve increases rapidly with the breakthrough time. It is clear that the longer the duration of the breakthrough time continued during the VOC adsorption process in the first stage, the higher the dynamic adsorption capacity exhibited.[54] ASMS-2 and SMS materials show the highest and lowest toluene adsorption capacity, respectively. The breakthrough times of all these as-obtained samples for toluene adsorption at the first phase match the following order: ASMS-2 (~42 min) > ASMS-3 (~36 min) > ASMS-1 (~24 min) > SMS (~12 min). Therefore, the dynamic toluene adsorption capacities[43] (q, mg g^{-1}) were in the order of SMS < ASMS-1 < ASMS-3 < ASMS-2 according to the adsorption capacity data listed in Table 3, and this result is well consistent with the nitrogen adsorption–desorption, especially the specific surface area. Compared with SMS, the adsorption capacities of ASMS are all increased, indicating that the amino functionalization treatment significantly increased the adsorption capacity of ASMS. This result can be explained by the combination of surface chemistry, pore volume and pore structure of the modified ASMS material.

3.3 Regeneration of ASMS-2 for toluene adsorption

Adsorption capacity and regeneration capacity are two important indexes to evaluate the adsorption performance of an adsorbent, whether in laboratory experiments or in engineering practice. As shown in Fig. 7, four cycles of dynamic toluene adsorption on ASMS-2 were studied and the fitting parameters of these four cycles are listed in Table 4. As shown in Fig. 7, the desorption operation of ASM-2, which was adsorption saturated, was carried out and four cycles of the dynamic adsorption were conducted. The parameters are listed in Table 4. ASMS-2 can be easily regenerated through thermal desorption and has good reproducibility in four dynamic toluene adsorption cycles. According to the dynamic toluene adsorption capacities, the recycling efficiency of ASMS-2 keeps steady, almost over 98%. Furthermore, according to the diffusion rate constants (k) and constant τ values, we found that the mass transfer and diffusion resistance of ASMS-2 showed no significant changes, indicating that the porous structure and surface chemical properties of ASMS-2 were well preserved during the four cycles of adsorption. Thus, ASMS-2 has high potential as an effective toluene adsorbent.

3.4 Mechanism of toluene adsorption

Previous studies have shown that the pore structure of a mesoporous material (such as specific surface area, pore size, *etc.*) and the interaction with the molecules of a pollutant gas (adsorption affinity) are two important factors affecting the adsorption capacity. In general, a larger specific surface area and a suitable pore size are more favorable for the adsorption of pollutant gas molecules. As one of the typical molecular sieve materials, SMS has the potential to exhibit physical adsorption and the adsorption process of toluene on SMS is largely physical adsorption. In the process of physical adsorption, the toluene gaseous molecules are transported to the outer surface in the form of convection diffusion as the gas flows through the
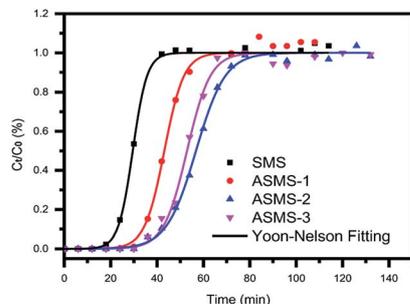
Fig. 6 Yoon–Nelson model of toluene adsorption on ASMS adsorbents.

Table 3 Dynamic adsorption capacity (q) and Yoon–Nelson equation parameters for toluene adsorption on ASMS adsorbents

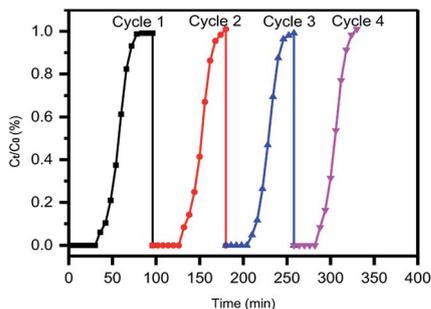|	Adsorption capacity			Yoon–Nelson parameters	
Sample	q' (mmol g^{-1})	q (mg g^{-1})	τ (min)	k	R^2
SMS	0.586	53.853	30	0.325	0.998
ASMS-1	0.912	83.770	43	0.237	0.995
ASMS-2	1.068	98.131	57	0.158	0.998
ASMS-3	0.977	89.754	53	0.204	0.995

Fig. 7 Cycles of toluene adsorption–desorption on ASMS-2.

Table 4 Yoon and Nelson equation parameters for various runs

Cycle	Adsorption capacity			Yoon–Nelson parameters	
	q' (mmol g^{-1})	q (mg g^{-1})	τ (min)	k	R^2
Run 1	1.055	96.934	57	0.159	0.998
Run 2	1.048	96.336	56	0.157	0.997
Run 3	1.035	95.139	49	0.164	0.999
Run 4	1.042	95.737	47	0.166	0.998

surface of the SMS adsorbent, and then the toluene molecules enter the inner pores from the outer surface of the SMS, thereby diffusing to the inner surface of the solid and are adsorbed. These two processes are called outer and inner diffusion, respectively, which are essentially surface adsorption processes. It can be obviously seen from Table 2 that although the specific surface area and pore diameter of the modified ASMS sample are smaller than those of the sample before the modification, the amount of toluene adsorbed by ASMS (up to 98.131 mg g^{-1}) is about 1.82 times that before the modification (53.853 mg g^{-1}), which means that in addition to traditional physical adsorption, the nature of the material surface also plays a significant role in promoting adsorption. Comparing the ability of the adsorbent to adsorb toluene before and after modification, it is evident that the strong interaction between the surface of ASMS and toluene is the major factor for increasing the gas adsorption capacity. According to the work by Zhao and colleagues, the silanol groups ($\equiv$Si–OH) on the pore surfaces of silica-based adsorbents act as the adsorption sites for various molecules,[55] and the hydroxyl groups present in the silica surface behave as weak acid sites interacting strongly with the π-electrons of toluene.[56] However, in our study, the strong interaction between toluene and the amino groups on the surface of ASMS-2 adsorbents might greater, which explains the phenomenon that ASMS-2 adsorbents have higher capacities than SMS adsorbents. In addition, due to the fact that most of the hydrophilic hydroxyl groups on the surface of SMS are replaced by –NH$_2$ during the modification process, the hydrophilicity of ASMS is decreased and the hydrophobicity is enhanced.[57,58] When hydrophobic toluene molecules are adsorbed onto the ASMS surface and into the pores, there must be some hydrophobic interaction between the two, which may

also be one of the favorable factors to increase the amount of toluene adsorption. Therefore, the ability of ASMS-2 to adsorb toluene is enhanced by the combination of the total pore volume the and the adsorption affinity,[59] and the gas adsorption capacity can be increased by grafting the amino groups onto the surface of the SMS in a suitable amount.

4. Conclusions

In this study, a novel ASMS material with a hydrophobic surface was obtained by post-synthesis modification. The conclusion is that the ASMS material is expected to be a potential adsorbent for low-concentration VOCs. Appropriate modification of the surface chemical groups of SBA-15 can improve its adsorption capacity to a certain extent. Obviously, ASMS could be a suitable adsorbent for toluene removal because of the high adsorption capacity and affinity. The experimental breakthrough data obtained for toluene adsorption were well fitted by the Yoon–Nelson mathematical model and stay well consistent with the breakthrough curves on ASMS-2. Particularly, the maximum toluene adsorption capacity can be obtained under an optimum mass ratio of APTES/TEOS, and an excessive or low mass ratio of APTES/TEOS will have a negative impact on the dynamic adsorption capacity. The results show that both the adsorption affinity and total pore volume of the adsorbent affect its adsorption capacity, and the synergistic effect between the two enhances the adsorption performance of the ASMS material, which makes it a good candidate for use in reducing industrial VOC emissions.

Conflicts of interest

There are no conflicts to declare.

Acknowledgements

References

1 M. Tancrède, R. Wilson, L. Zeise and E. A. C. Crouch, *Atmos. Environ.*, 1987, **21**, 2187–2205.

2 M. A. Lillo-Ródenas, D. Cazorla-Amorós and A. Linares-Solano, *Carbon*, 2005, **43**, 1758–1767.

3 W. P. L. Carter, D. R. C. Iii, D. R. Fitz, I. L. Malkina, K. Bumiller, C. G. Sauer, J. T. Pisano, C. Bufalino and C. Song, *Atmos. Environ.*, 2005, **39**, 7768–7788.

4 A. Hartikainen, P. Yli-Pirilä, P. Tiitta, A. Leskinen, M. Kortelainen, J. Orasche, J. Schnelle-Kreis, L. Kej, R. Zimmermann and J. Jokiniemi, *Environ. Sci. Technol.*, 2018, **52**, 4979.

5 Z. Du, J. Mo, Y. Zhang and Q. Xu, *Building and Environment*, 2014, **72**, 75–81.

6 M. J. Mendell, *Indoor Air*, 2007, **17**, 259–277.

7 F. I. Khan and A. K. Ghoshal, *J. Loss Prev. Process Ind.*, 2000, **13**, 527–545.

8 Y. Wang, X. Su, Z. Xu, K. Wen, P. Zhang, J. Zhu and H. He, *Appl. Surf. Sci.*, 2016, **363**, 113–121.

9 A. Anfruns, M. J. Martin and M. A. Montes-Morán, *Chem. Eng. J.*, 2011, **166**, 1022–1031.

10 X. Liang, F. Qi, P. Liu, G. Wei, X. Su, L. Ma, H. He, X. Lin, Y. Xi and J. Zhu, *Appl. Clay Sci.*, 2016, **132–133**, 96–104.

11 P. Liu, H. He, G. Wei, X. Liang, F. Qi, F. Tan, T. Wei, J. Zhu and R. Zhu, *Appl. Catal., B*, 2016, **182**, 476–484.

12 Y. Cheng, H. He, C. Yang, G. Zeng, X. Li, H. Chen and G. Yu, *Biotechnol. Adv.*, 2016, **34**, 1091–1102.

13 J. M. Estrada, S. Hernández, R. Muñoz and S. Revah, *J. Hazard. Mater.*, 2013, **250–251**, 190–197.

14 Y. F. Guo, D. Q. Ye, K. F. Chen and J. C. He, *Catal. Today*, 2007, **126**, 328–337.

15 V. K. Gupta and N. Verma, *Chem. Eng. Sci.*, 2002, **57**, 2679–2696.

16 S. W. Baek, J. R. Kim and S. K. Ihm, *Catal. Today*, 2004, **93–95**, 575–581.

17 A. N. Zagoruiko, V. V. Mokrinskii, S. A. Veniaminov and A. S. Noskov, *J. Environ. Chem. Eng.*, 2017, **5**, 5850–5856.

18 Y. Cao, J. Wang, J. Qiao, H. Wan, H. Li and J. Zhu, *Acta Chim. Sin.*, 2013, **71**, 567.

19 N. P. Tangale, A. A. Belhekar, K. B. Kale and S. V. Awate, *Water, Air, Soil Pollut.*, 2014, **225**, 1847.

20 D. Ludgen, H. Wichmann and M. Bahadir, *Clean: Soil, Air, Water*, 2013, **41**, 743–750.

21 A. A. Assadi, J. Palau, A. Bouzaza, J. Penya-Roja, V. Martinez-Soriac and D. Wolbert, *J. Photochem. Photobiol., A*, 2014, **282**, 1–8.

22 F. Thevenet, O. Guaitella, E. Puzenat, J. M. Herrmann, A. Rousseau and C. Guillard, *Catal. Today*, 2007, **122**, 186–194.

23 D. T. Tefera, Z. Hashisho, J. H. Philips, J. E. Anderson and M. Nichols, *Environ. Sci. Technol.*, 2014, **48**, 5108–5117.

24 X. Zhang, B. Gao, Y. Zheng, X. Hu, A. E. Creamer, M. D. Annable and Y. Li, *Bioresour. Technol.*, 2017, **245**, 606.

25 D. T. Tefera, L. M. Jahandar, M. Fayaz, Z. Hashisho, J. H. Philips, J. E. Anderson and M. Nichols, *Environ. Sci. Technol.*, 2013, **47**, 11700.

26 J. Qi, Y. Li, G. Wei, J. Li, X. Sun, J. Shen, W. Han and L. Wang, *Sep. Purif. Technol.*, 2017, **188**, 112–118.

27 M. I. Konggidinata, B. Chao, Q. Lian, R. Subramaniam, M. Zappi and D. D. Gang, *J. Hazard. Mater.*, 2017, **336**, 249–259.

28 G. Zhang, Y. F. Zhang and L. Fang, *Indoor Air*, 2008, **18**, 37–43.

29 A. A. Christy, *Ind. Eng. Chem. Res.*, 2011, **50**, 5543–5549.

30 Y. Zhou, L. Zhou, X. Zhang and Y. Chen, *Microporous Mesoporous Mater.*, 2016, **225**, 488–493.

31 K. Vellingiri, P. Kumar, A. Deep and K. H. Kim, *Chem. Eng. J.*, 2016, **307**, 1116–1126.

32 M. Qiu, C. Chen and W. Li, *Catal. Today*, 2015, **258**, 132–138.

33 D. P. Serrano, G. Calleja, J. A. Botas and F. J. Gutierrez, *Ind. Eng. Chem. Res.*, 2004, **43**, 7010–7018.

34 M. S. Hussein and M. J. Ahmed, *Mater. Chem. Phys.*, 2016, **181**, 512–517.

35 D. Xu, J. Ma, H. Zhao, Z. Liu and R. Li, *Fluid Phase Equilib.*, 2016, **423**, 8–16.

36 R. Serna-Guerrero and A. Sayari, *Environ. Sci. Technol.*, 2007, **41**, 4761–4766.

37 D. Zhao, J. Feng, Q. Huo, N. Melosh, G. H. Fredrickson, B. F. Chmelka and G. D. Stucky, *Science*, 1998, **279**, 548–552.

38 M. Hasanzadeh, N. Shadjou, M. D. L. Guardia, M. Eskandani and P. Sheikhzadeh, *Trends Anal. Chem.*, 2012, **33**, 117–129.

39 C. Chen, S. Zhang, K. H. Row and W. S. Ahn, *J. Energy Chem.*, 2017, **26**, 868–880.

40 E. Vunain, A. K. Mishra and B. B. Mamba, *Int. J. Biol. Macromol.*, 2016, **86**, 570–586.

41 Y. Zhou, G. Quan, Q. Wu, X. Zhang, B. Niu, B. Wu, Y. Huang, X. Pan and C. Wu, *Acta Pharm. Sin. B*, 2018, **8**, 165–177.

42 Q. Hu, J. J. Li, Z. P. Hao, L. D. Li and S. Z. Qiao, *Chem. Eng. J.*, 2009, **149**, 281–288.

43 J. Zhu, P. Zhang, Y. Wang, K. Wen, X. Su, R. Zhu, H. He and Y. Xi, *Appl. Clay Sci.*, 2018, **159**, 60–67.

44 F. Qu, G. Zhu, H. Lin, W. Zhang, J. Sun, S. Li and S. Qiu, *J. Solid State Chem.*, 2006, **179**, 2027–2035.

45 B. S. Tian and C. Yang, *J. Nanosci. Nanotechnol.*, 2011, **11**, 1871–1879.

46 T. P. B. Nguyen, J. W. Lee, G. S. Wang and H. Moon, *Microporous Mesoporous Mater.*, 2008, **110**, 560–569.

47 E. Da'Na, *Microporous Mesoporous Mater.*, 2017, **145**, 145–157.

48 S. Jin, B. C. Park, W. S. Ham, L. Pan and Y. K. Kim, *Colloids Surf., A*, 2017, **531**, 133–140.

49 G. Li, B. Wang, Q. Sun, W. Xu and Y. Han, *Microporous Mesoporous Mater.*, 2017, **252**, 105–115.

50 B. S. Tian and C. Yang, *J. Phys. Chem. C*, 2015, **113**, 4925–4931.

51 K. Kosuge, S. Kubo, N. Kikukawa and M. Takemori, *Langmuir*, 2007, **23**, 3095–3102.

52 Y. H. Yoon and J. H. Nelson, *Am. Ind. Hyg. Assoc. J.*, 1984, **45**, 517–524.

53 Z. H. Huang, F. Kang, K. M. Liang and J. Hao, *J. Hazard. Mater.*, 2003, **98**, 107–115.

54 B. Dou, Q. Hu, J. Li, S. Qiao and Z. Hao, *J. Hazard. Mater.*, 2011, **186**, 1615–1624.

55 X. S. Zhao, G. Q. Lu and X. Hu, *Colloids Surf., A*, 2001, **179**, 261–269.

56 S. G. Rodrigo and S. Abdelhamid, *Environ. Sci. Technol.*, 2007, **41**, 4761–4766.

57 S. Wang, *Microporous Mesoporous Mater.*, 2009, **117**, 1–9.

58 J. M. Rosenholm and L. Mika, *J. Controlled Release*, 2008, **128**, 157–164.

59 Q. Hu, J. J. Li, Z. P. Hao, L. D. Li and S. Z. Qiao, *Chem. Eng. J.*, 2009, **149**, 281–288.